Solid State Sciences 99 (2020) 106008

Contents lists available at ScienceDirect

Solid State Sciences

journal homepage: www.elsevier.com/locate/ssscie

Crystal structure and magnetic properties of $Sr_2Ni_{1-x}Mg_xMoO_6$ (x = 0, 0.25, 0.5, and 0.75) polycrystals

N. Urusova[a,b,*], M. Rajesh Kumar[a], M. Semkin[a,f], E. Filonova[a], M. Kratochvilova[c,d,e], D. Neznakhin[a], K. Grzhegorzhevskii[a], A. Ostroushko[a], J.-G. Park[c,d], A. Pirogov[a,f]

[a] Institute of Natural Sciences of the Ural Federal University, Ekaterinburg, Russia
[b] Institute of Solid State Chemistry of the Ural Branch of the RAS, Ekaterinburg, Russia
[c] Center for Correlated Electron Systems, Institute for Basic Science, Seoul, South Korea
[d] Department of Physics and Astronomy, Seoul National University, Seoul, South Korea
[e] Faculty of Mathematics and Physics, Charles University, Prague, Czech Republic
[f] M.N. Mikheev Institute of Metal Physics of the Ural Branch of the RAS, Ekaterinburg, Russia

ARTICLE INFO

Keywords:
Antiferromagnet
Paramagnet
Crystal structure
Raman spectroscopy
Magnetic susceptibility
Double perovskite

ABSTRACT

$Sr_2Ni_{1-x}Mg_xMoO_6$ double perovskites were synthesized by pyrolysis of glycerol–salt mixtures and their vibrational phonon modes were investigated using optical spectroscopic techniques. X-ray diffraction and Raman spectroscopy were employed to investigate crystal structures of these perovskite materials and purity of the samples. The magnetic ground state of $Sr_2Ni_{1-x}Mg_xMoO_6$ has been characterized using magnetic susceptibility measurements indicating that $Sr_2Ni_{0.75}Mg_{0.25}MoO_6$ orders in an antiferromagnetic state at about 56 K while $Sr_2Ni_{0.5}Mg_{0.5}MoO_6$ and $Sr_2Ni_{0.25}Mg_{0.75}MoO_6$ are paramagnetic.

1. Introduction

Complex oxides, which crystallize in the double perovskite structure, arouse the wide interest of researchers due to the large variety of electrical, magnetic, and catalytic properties. These compounds can be described by the general formula $A_2BB'O_6$, where A = (Sr, Ca, Ba) is an alkaline earth metal; B = (Fe, Co, Ni, Cr, etc.) is 3d transition metal and B' = (Mo, W, Re, U) is the diamagnetic hexavalent ions [1–3]. In these materials at position B there can be both magnetic and non-magnetic ions, because of this, the interaction occurs indirectly through the B–O–B'–O–B bonds [3,4]. In double perovskites of type $A_2BB'O_6$, the B ions can interact with each other as through direct and super-exchange interactions. Super-exchange interaction will be dominant, while direct exchange will be negligible due to the large distance between the B ions [3]. Most of the compounds from the $A_2BB'O_6$ family are low-temperature antiferromagnets [5–7], except Sr_2FeMoO_6 – a ferrimagnet at temperatures above room [4] and La_2BMnO_6 B = (Mg, Co, Ni) – a ferromagnetic [8].

Due to the wide variety of A, B and B' ions contained in $A_2BB'O_6$, these materials exhibit a large amount of properties, such as, Sr_2FeMoO_6 has a colossal magnetoresistance [9], Sr_2CrWO_6 has a half-metallicity effect [10], and Sr_2NiMoO_6 is multiferroic [6,11].

In the ground state, compounds based on Sr_2BMoO_6 crystallize in a tetragonal structure (space group $I4/m$), then, as the temperature rises, a structural phase transition to a cubic structure occurs (space group Fm-$3m$). For example, in the Sr_2CoMoO_6 compound, the structural phase transition occurs at a temperature of T = 560 K [5]. In addition, the temperature of both structural and magnetic phase transitions can be purposefully changed with the help of partial or complete substitution of 3d-transition B = (Ni, Co, Fe, Mn) metals.

Sr_2NiMoO_6 double perovskite and derived compounds are intensively studied systems [6]. They have a number of physical and chemical properties that open up the prospect of their widespread use and studies of fundamental properties. First, double-perovskite-based compounds are considered as the basis for the anode of solid oxide fuel cells (SOFC). SOFC are promising electrochemical devices that convert chemical energy of fuel into electrical energy, with a high degree of energy conversion. These cells are also characterized lack of noise, and low levels of environmental pollution [12].

To increase the electrical conductivity, chemical and thermal stability, and compatibility with the electrolyte based on lanthanum gallate, the Sr_2NiMoO_6 compound is alloyed with both strontium and nickel sublattices [13–16].

Moreover, the Sr_2NiMoO_6-based compounds reveal multiferroic

* Corresponding author. Institute of Natural Sciences of the Ural Federal University, Ekaterinburg, Russia.
E-mail address: natalia.urusova@urfu.ru (N. Urusova).

https://doi.org/10.1016/j.solidstatesciences.2019.106008
Received 10 July 2019; Received in revised form 13 September 2019; Accepted 15 September 2019
Available online 18 September 2019

properties [6], opening up broad technological applications in the field of magnetic field sensors [17,18], for recording and storing information, as well as in spintronics. Sr_2NiMoO_6 is a *B*-ordered with a double perovskite structure, in which the magnetic ion Ni^{2+} occupies position *B*, while the diamagnetic ion Mo^{6+} occupies position *B′*. Its crystal structure at room temperature, like most of the Sr_2BMoO_6 family, is tetragonal and transforms to the cubic symmetry above 550 K [6].

The aim of this paper is to study effects of the partial substitution of Ni by Mg on the crystal structure and magnetic properties of $Sr_2Ni_{1-x}Mg_xMoO_6$.

2. Experimental

2.1. Synthesis of $Sr_2Ni_{1-x}Mg_xMoO_6$ double perovskites

The polycrystalline $Sr_2Ni_{1-x}Mg_xMoO_6$ samples (x = 0, 0.25, 0.5, and 0.75) were synthesized via the pyrolysis of glycerol-salt solutions, which was chosen as the most optimal according to the conclusions of our work [19], modified by the addition of ammonium nitrate [20] as a process combustion activator. The stoichiometric amounts of magnesium oxide MgO, nickel acetate $Ni(CH_3COO)_2{\cdot}4H_2O$, and strontium carbonate $SrCO_3$ with purity not less than 99.5% were dissolved in dilute nitric acid HNO_3. The resulting solution was transferred to a porcelain dish, and then the previously prepared solution of ammonium heptamolybdate $(NH_4)_6Mo_7O_{24}{\cdot}4H_2O$ in distilled water was added. The solution containing the salts of the starting metals was kept at 353 K for 6 h to ensure the mixing of metal cations at the molecular level. The ammonium nitrate NH_4NO_3 as a compound with the high exothermal effect and glycerol as an organic fuel (in the mass proportion 3:10) were added to the resulting solution. The resulting mixtures were heated on the plate to the auto combustion and dryness. The powders were annealed in air progressively at temperatures of 1173, 1273, and 1373 K for 24 h with intermediate milling in ethanol. The heating/cooling rate of the furnace was 200 K/hour. At the final stage, the samples were quenched from $T = 1373$ K to room temperature at a rate of 300 K/min.

2.2. Characterization

X-ray diffraction (XRD) measurements were performed with BRUKER D8 Advance high-resolution X-ray diffractometer at Seoul National University and Inel Equinox 3000 at Ural Federal University using a Bragg-Brentano geometry with a Cu $K_{\alpha1,2}$ source (wavelength $\lambda_1 = 1.540510$ Å and $\lambda_2 = 1.54422$ Å) at 298 K.

Neutron powder diffraction (NPD) patterns were obtained at room temperature on the D2 diffractometer, installed on a horizontal channel of the WWR-2M reactor (Zarechny, Russia), with the neutron wavelength of $\lambda = 1.805$ Å. Structural parameters were refined by Rietveld method using Fullprof program [21]. The crystal structure was visualized with VESTA computer program [22].

The crystal structure of the as-prepared samples was analyzed of using Raman Spectroscopy. Raman measurements were performed on Confocal Raman microscope Alpha 300 AR (WITec GmbH, Germany) equipped with He–Ne laser with maximum power 35 mW. The laser radiation was focused at the sample via 100x objective (NA = 0.75) and scattered light was expanded into the spectrum by diffraction grating with 600 lines/mm providing spectral resolution better than 2 cm^{-1}. A 50 μm diameter optical fiber was used as a confocal pinhole. Excitation laser wavelength is 488 nm.

Magnetic measurements were performed with the Magnetic Property Measurement System (MPMS XL-7) in the temperature range (2–300) K, under the applied magnetic field of 1 kOe, in the zero-field cooled (ZFC) and the field cooled (FC) modes at the Ural Federal University. The magnetization vs magnetic field curves were obtained for magnetic fields region ± 70 kOe at 2 and 300 K.

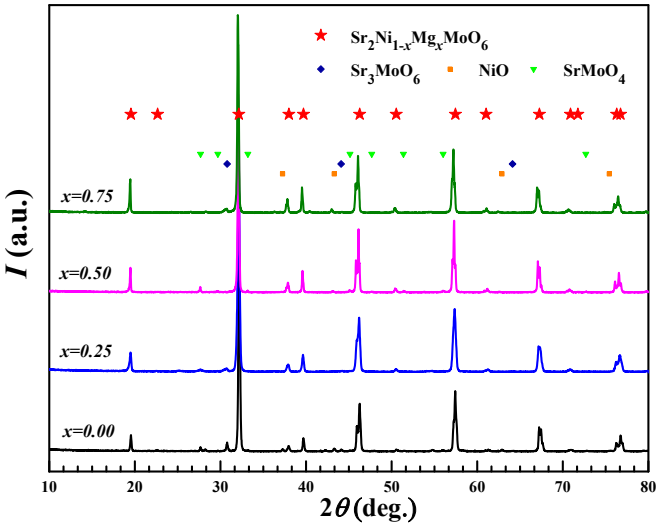

Fig. 1. X-ray diffraction patterns of the $Sr_2Ni_{1-x}Mg_xMoO_6$ (x = 0, 0.25, 0.5, and 0.75) samples at room temperature.

3. Results and discussion

3.1. Structural and morphological studies

Fig. 1 shows the X-ray diffraction patterns of Sr_2NiMoO_6, $Sr_2Ni_{0.75}Mg_{0.25}MoO_6$, $Sr_2Ni_{0.5}Mg_{0.5}MoO_6$, and $Sr_2Ni_{0.25}Mg_{0.75}MoO_6$ obtained at 298 K. According to the X-ray diffraction data, the $Sr_2Ni_{1-x}Mg_xMoO_6$ (x = 0, 0.25, 0.5, and 0.75) samples contain no more than 5 wt % of impurity phases, such as: $SrMoO_4$, Sr_3MoO_6, and NiO. The presence of such the impurities is a feature of the synthesis of a family Sr_2BMoO_6 *B* = (Mg, Fe, Mn, Ni, Co) double perovskite [1,23]. In accordance with the X-ray data, a doping of Sr_2NiMoO_6 (impurity content is about 5 wt %) for magnesium ions, allows lowering the impurity content (about 2 wt %).

Refinement of the structural parameters of the $Sr_2Ni_{1-x}Mg_xMoO_6$ (x = 0, 0.25, 0.5, and 0.75) samples revealed that their crystal structure is described a tetragonal cell (space group *I4/m*) isostructural to that of pure Sr_2NiMoO_6. These crystallographic data for $Sr_2Ni_{1-x}Mg_xMoO_6$ (x = 0, 0.25, and 0.5) confirm results given in our previous work [24]. But, now the structure for x = 0.75 is described by also tetragonal space group that is in contrast to Ref. [25], where we use a trigonal cell (space group *I*-1). This fact points the microstructure and crystalline structure of the samples strongly depends on the synthesis route; in particular, from the composition of the redox pyrolysis mixture as shown earlier in Ref. [19]. As we will show below, the present data for the $Sr_2Ni_{0.25}Mg_{0.75}MoO_6$ composition is confirmed by the Raman scattering.

As an example, experimental and calculated X-ray $Sr_2Ni_{0.5}Mg_{0.5}MoO_6$ patterns are shown in Fig. 2. Refined unit cell constants, atomic coordinates, and agreement factors are listed in Table 1. Refined values are in agreement with the data given in literature [6,25]. The best agreement between the experimental and calculated values is achieved by the following structural parameters: Sr^+ ions occupy the 4*d* position with coordinates (0, 0.5, 0.25), Ni^{2+}/Mg^{2+} ions occupy 2*b* position with coordinates (0, 0.5, 0), Mo^{6+} ions are in position 2*a* (0, 0, 0), and O^{2-} ions located at nodes 8*h* (*x*, *y*, 0) and 4*e* (0, 0, *z*). In Fig. 2, the inset shows the crystal structure of $Sr_2Ni_{0.5}Mg_{0.5}MoO_6$. The Sr^{2+}, Ni/Mg^{2+}, Mo^{6+}, and O^{2-} ions are represented by yellow, green/purple, blue, and red spheres.

For two (Sr_2NiMoO_6 and $Sr_2Ni_{0.75}Mg_{0.25}MoO_6$) samples neutron diffraction measurements were performed (see Fig. 3). These measurements were carried out to determine the position occupation coefficients for oxygen ions, as given in Table 1. The use of neutron

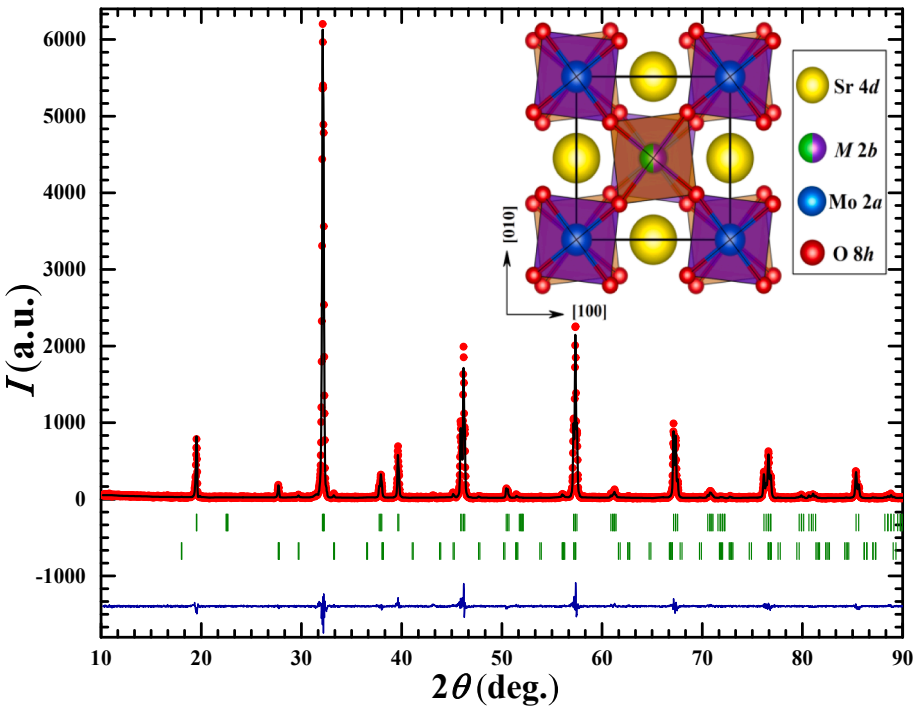

Fig. 2. Observed (points) and calculated (line) XRD patterns of $Sr_2Ni_{0.5}Mg_{0.5}MoO_6$ at room temperature. The first row of the vertical bars is the Bragg reflection positions of the main phase; the second row – the impurity phase $SrMoO_4$. The difference between calculated and observed intensities is shown at the bottom as solid line.

diffraction is justified by the presence of light atoms, such as oxygen, whose occupation coefficients cannot be determined X-ray diffraction with a high degree of confidence. Using the neutron and X-ray data about the atom coordinates and the lattice parameters, the interatomic distances were calculated for all materials. They are given in Table 2.

According to Tables 1 and 2, the unit cell parameters and the molar volume, and interatomic distances increase with increasing doping of nickel ions with magnesium ions in the $Sr_2Ni_{1-x}Mg_xMoO_6$ due to the size effect: the ionic radii of Ni_{VI}^{2+} and Mg_{VI}^{2+} are 0.69 and 0.72 Å, respectively [26]. The crystallographic data of $Sr_2Ni_{1-x}Mg_xMoO_6$ are in a good agreement with our previous works [19,25] and literature [6,15,27].

3.2. Raman analysis

In general, $A_2BB'O_6$, cation ordering and tilting of the oxygen octahedra are the main structural features. A higher degree of order is expected if there is a larger difference in the sizes of *B* and *B′* ions and their valence states [28,29]. Usually X-ray diffraction is used to detect the degree of *B*-site order in complex-perovskite materials, whereas recent studies proved that Raman scattering is an ideal tool for probing the degree of *B*-site order in complex perovskites [30–32]. Tolerance factor determines the properties of perovskite type oxides. Theoretically, the tolerance factor $t \geq 1$ for ferroelectric perovskites and $t < 1$ for antiferroelectric perovskites. However, Goldschmidt [33] found

Table 1
Crystallographic data of $Sr_2Ni_{1-x}Mg_xMoO_6$ (x = 0, 0.25, 0.5, and 0.75) at 298 K. All ion sites are fully occupied. Parameters *a*, *b*, *c*, and *V* are the constants of the unit cell and its volume; *x*, *y*, and *z* are the refined ion coordinates; 4*d*, 2*b*, 2*a*, 8*h*, and 4*e* are Wyckoff symbols. R_f and χ^2 are Bragg and global agreement factors, respectively.

Parameter	Sr_2NiMoO_6	$Sr_2Ni_{0.75}Mg_{0.25}MoO_6$	$Sr_2Ni_{0.5}Mg_{0.5}MoO_6$	$Sr_2Ni_{0.25}Mg_{0.75}MoO_6$
a, Å	5.5463(3)	5.5471(1)	5.5568(2)	5.5619(3)
c, Å	7.8923(6)	7.8926(2)	7.9048(3)	7.9094(4)
V, Å^3	242.28(3)	242.78(1)	244.08(1)	244.69(2)
		Sr 4*d* (0, 1/2, 1/4)		
Occ (Sr)	0.25(2)	0.232(3)	0.225(6)	0.237(9)
		Ni(Mg) 2*b* (0, 0, 1/2)		
Occ (Ni)	0.126(7)	0.089(1)	0.061(1)	0.033(2)
Occ (Mg)	0.000(1)	0.027(1)	0.061(1)	0.096(2)
		Mo 2*a* (0, 0, 0)		
Occ (Mo)	0.126(7)	0.114(1)	0.112(2)	0.117(4)
		O1 8*h* (*x*, *y*, 0)		
x	0.271(5)	0.272(2)	0.279(2)	0.280(2)
y	0.211(6)	0.206(2)	0.204(2)	0.204(3)
Occ (O1)	0.539(3)	0.498(2)	0.51(2)	0.50(1)
		O2 4*e* (0, 0, *z*)		
z	0.240(3)	0.239(2)	0.253(2)	0.250(2)
Occ (O2)	0.229(2)	0.252(1)	0.25(1)	0.25(1)
R_f, %	1.38	2.79	4.30	4.38
χ^2, %	1.89	2.99	4.19	5.10

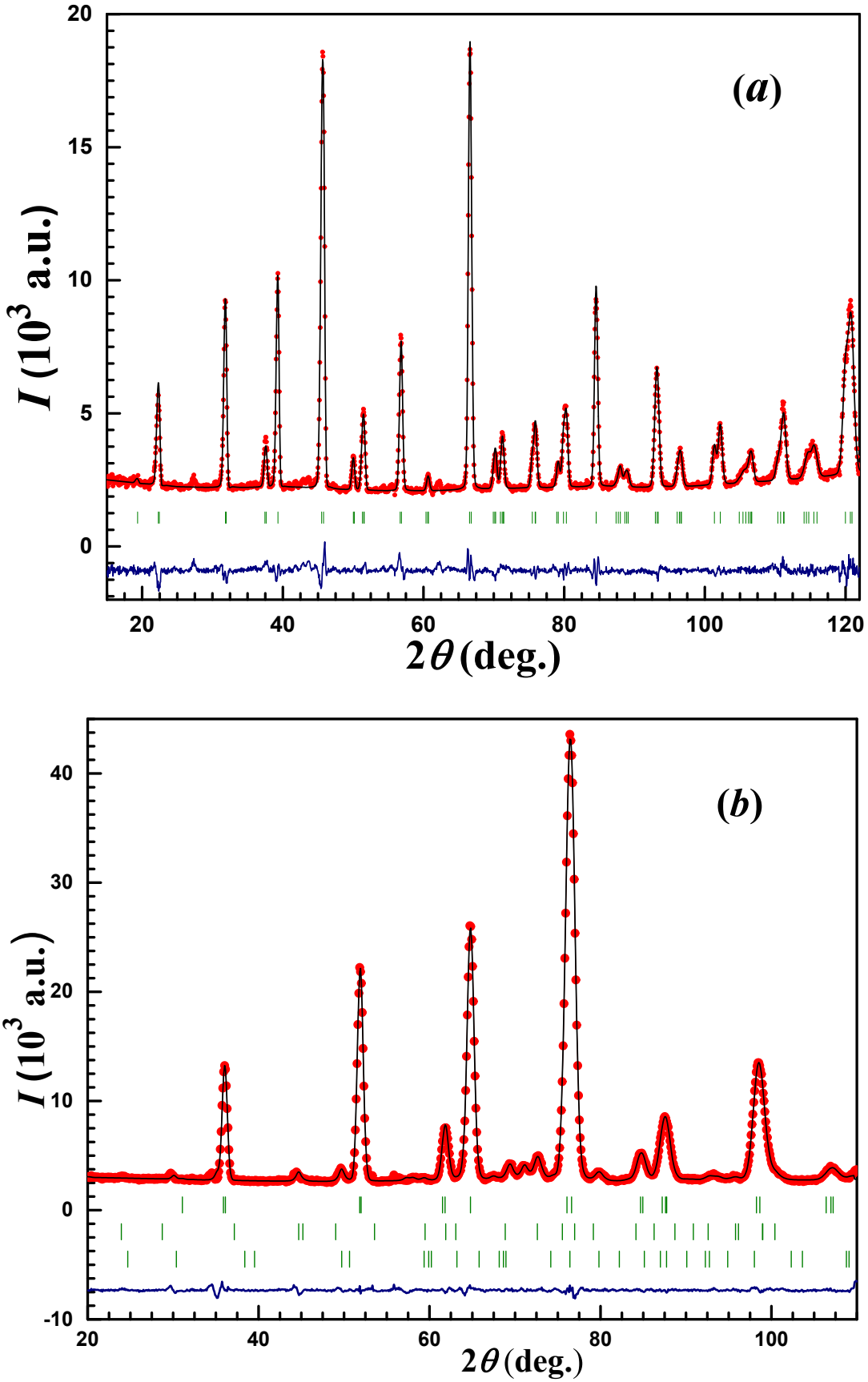

Fig. 3. Observed (points) and calculated (line) NPD patterns of Sr_2NiMoO_6 (*a*) and $Sr_2Ni_{0.75}Mg_{0.25}MoO_6$ (*b*) at room temperature. The first row of the vertical bars is the Bragg reflection positions of the main phase; the second and third rows – the impurity phases $SrMoO_4$ and Sr_3MoO_6, respectively. The difference between calculated and observed intensities is shown at the bottom as solid line.

Table 2
Interatomic distances and bond valence sums for $Sr_2Ni_{1-x}Mg_xMoO_6$ (x = 0, 0.25, 0.5, and 0.75) at 298 K.

Parameter	Sr_2NiMoO_6	$Sr_2Ni_{0.75}Mg_{0.25}MoO_6$	$Sr_2Ni_{0.5}Mg_{0.5}MoO_6$	$Sr_2Ni_{0.25}Mg_{0.75}MoO_6$
Sr–O1	2.95(2)	2.989(7)	2.578(6)	2.574(8)
Sr–O1	2.62(2)	2.590(6)	2.578(6)	2.574(9)
Sr–O2	2.7743(9)	2.7752(5)	2.7785(1)	2.7810(1)
Ni(Mg)–O1	2.05(3)	2.04(1)	2.04(1)	2.04(2)
Ni(Mg)–O2	2.05(3)	2.07(1)	1.96(1)	1.99(2)
Mo–O1	1.91(3)	1.92(1)	1.94(1)	1.95(2)
Mo–O2	1.89(3)	1.88(1)	1.99(1)	1.97(2)

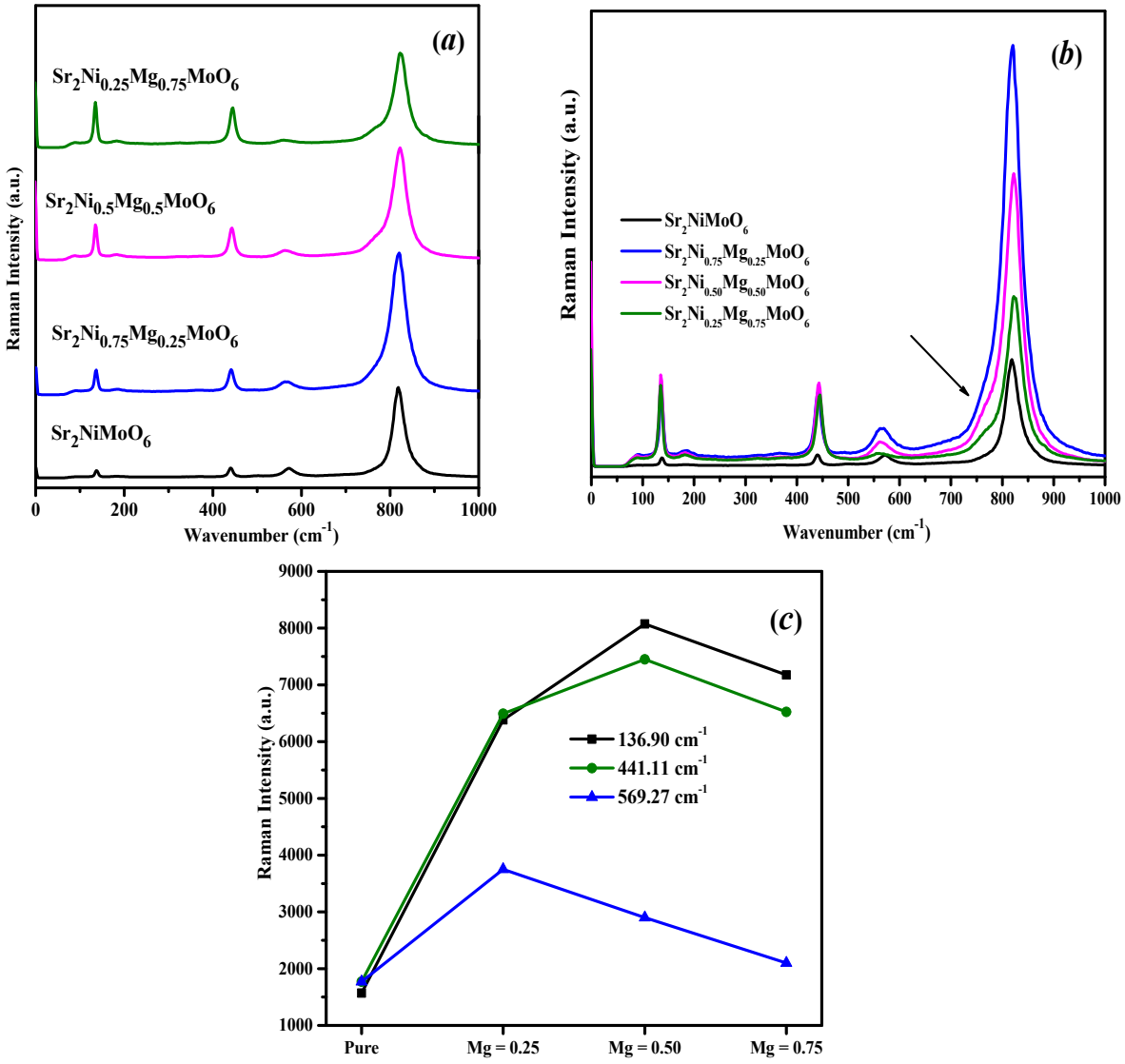

Fig. 4. Raman spectra of $Sr_2Ni_{1-x}Mg_xMoO_6$ (x = 0, 0.25, 0.50, and 0.75) in the range (0–1000) cm^{-1} (*a*), overlapping Raman spectra of $Sr_2Ni_{1-x}Mg_xMoO_6$ (x = 0, 0.25, 0.50, and 0.75) (*b*) and changes of Raman intensity in the $Sr_2Ni_{1-x}Mg_xMoO_6$ (x = 0, 0.25, 0.50, and 0.75) samples (*c*).

that, as an experimental fact, *t* values of most ideal perovskite structures are in the range of (0.8–0.9), and distorted perovskite structures occur in somewhat wider range of *t*. The calculated *t* range of our samples is in between (0.9–1.0) and corresponds to antiferroelectric perovskites. The calculated tolerance factor values are 0.9542, 0.9525, 0.9508, and 0.9491 for Sr_2NiMoO_6, $Sr_2Ni_{0.75}Mg_{0.25}MoO_6$, $Sr_2Ni_{0.50}Mg_{0.50}MoO_6$, and $Sr_2Ni_{0.25}Mg_{0.75}MoO_6$, respectively.

According to our previous articles and literature data, the mixed oxides with the double perovskite structure can be prepared in air: Sr_2NiMoO_6 [1,6] shows a tetragonal structure with space group *I4/m* at 298 K and undergoes a tetragonal-to-cubic phase transition at high temperatures [23,34]. Fig. 4*a* shows the Raman spectra of $Sr_2Ni_{1-x}Mg_xMoO_6$ (x = 0, 0.25, 0.50, and 0.75) in the range (0–1000) cm^{-1}. For complex-perovskite materials, the active modes of Raman spectra are given as:

$$\Gamma = A_{1g} + E_g + 2T_{2g} \quad (1)$$

In total, four peaks are observed in a complex-perovskite system.

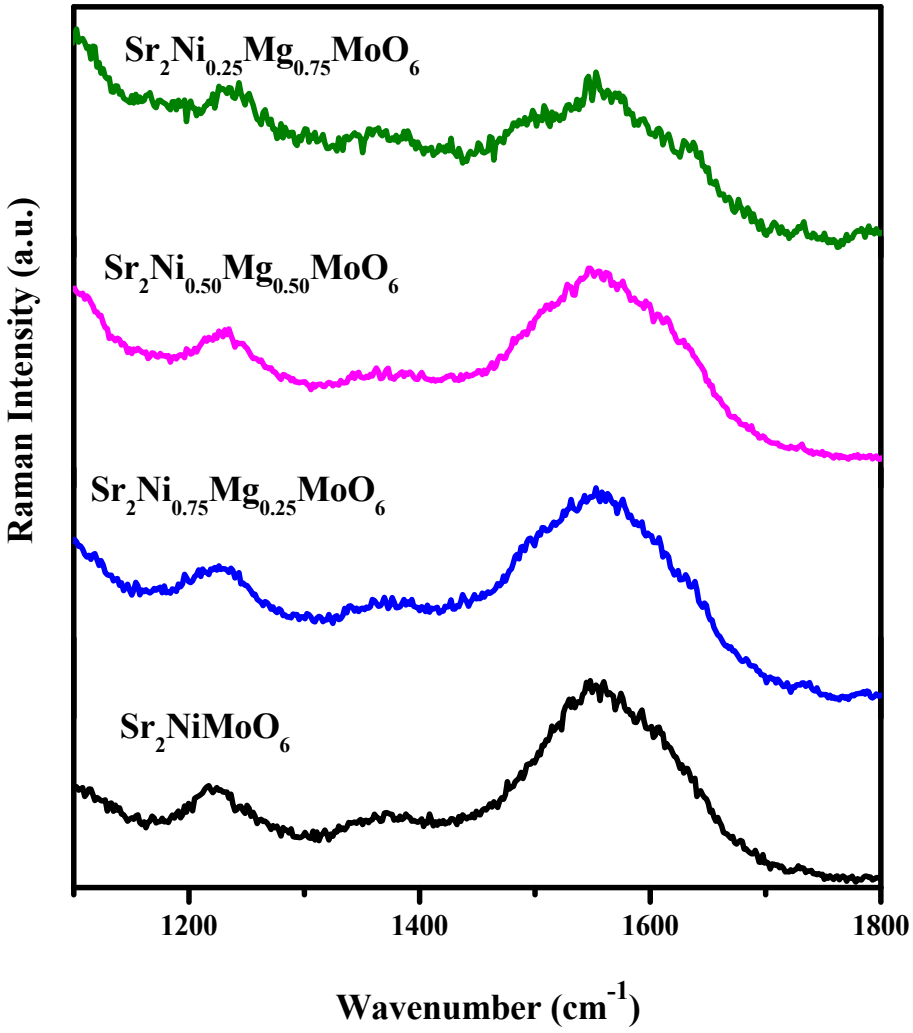

Fig. 5. Raman spectra of $Sr_2Ni_{1-x}Mg_xMoO_6$ (x = 0, 0.25, 0.50, and 0.75) in the range (1100–1800) cm^{-1}

From Fig. 4*a*, we observe the strong major narrow peak (A_{1g}) at around 818 cm^{-1} and three minor peaks ($T_{2g(1)}$, $T_{2g(2)}$ and E_g) at low frequency regions around 130, 440, and 560 cm^{-1}, respectively. In general, the broad structure in the frequency range (700–850) cm^{-1} can be taken as an indicator of the presence of an amorphous or highly disordered $SrMoO_4$ phase at the grain surfaces of the material. The strong major peaks (A_{1g}) observed in the $Sr_2Ni_{1-x}Mg_xMoO_6$ (x = 0, 0.25, 0.50, and 0.75) samples are at around 818.61, 820.17, 822.17, and 823.22 cm^{-1} corresponding to the internal stretching modes of the $SrMoO_4$ phase. The two low-range peaks are observed at around 137.48, 136.43, 134.67, 134.67 cm^{-1}, and 440.14, 441.13, 443.01, 445.03 cm^{-1} which confirms the presence of Sr_2NiMoO_6 phase in the $Sr_2Ni_{1-x}Mg_xMoO_6$ (x = 0, 0.25, 0.50, and 0.75) samples. Shifting in the Raman spectra (A_{1g}, $T_{2g(1)}$ and $T_{2g(2)}$) occurs with increasing percentage of magnesium due to (i) lower atomic weight in comparison with nickel and (ii) a shift is an increase in *O–B–*O bond order, which is consistent with the observed decrease in the Mo–O bond distance when going from the tetragonal to triclinic structure [35].

The peak observed at about 572.66, 565.73, 561.68, and 559.66 cm^{-1} indicates two possibilities: (i) another kind of (NiO) impurity is present also in the $Sr_2Ni_{1-x}Mg_xMoO_6$ (x = 0, 0.25, 0.50, and 0.75) samples and the peak intensity decreases while increasing the doping (Mg) concentration. The band at 1490 cm^{-1} is due to a two-magnon (2 M) scattering on NiO [36]. The two-magnon (2 M) band experiences significant decrease of intensity with increase in Mg concentration. This effect can be explained by a decrease of antiferromagnetic spin correlations [37] leading to the antiferromagnetic-to-paramagnetic transition. (ii) E_g peak, whereas the changes in the intensity of Eg peak indicate the structural transition from the tetragonal to triclinic phase. Another peak observed around 776 cm^{-1} (shown in Fig. 4*b*), which is probably not totally symmetric, arises from an anharmonic component, whose effect increases when going from the tetragonal to triclinic structure [24].

As seen in Fig. 4*a*, significant differences of the intensity values are observed (with and without Mg) in the $Sr_2Ni_{1-x}Mg_xMoO_6$ (x = 0, 0.25, 0.50, and 0.75) samples. In general, Raman intensity is mainly affected by four factors: the direct proportion upon of the light source intensity, the dependence $1/(\lambda^4)$ upon of the source wave length, the sample quantity, and the sample scattering properties. In this work, the Raman intensity increased when adding Mg in the sample composition and decreased further with an increase of doping concentration due to size difference of the B-site ions. The size of Mg_{VI}^{2+} (0.72 Å) is slightly higher than Ni_{VI}^{2+} (0.69 Å) and Mo_{VI}^{2+} (0.69 Å) [38] which leads the structural changes from tetragonal (Sr_2NiMoO_6) to triclinic ($Sr_2Ni_{1-x}Mg_xMoO_6$, x = 0.25, 0.5, and 0.75). The increase of doping concentration having larger size must cause the structural changes and it is also indicated in the Raman intensity. Fig. 4*c* shows the comparison of changes in intensities of the $Sr_2Ni_{1-x}Mg_xMoO_6$ (x = 0, 0.25, 0.50, and 0.75) Raman spectra. Namely, the intensity increases after the partial substitution of Ni by Mg. Since the intensity allows evaluating the distortions of the crystal structure, it clearly shows that the doping and associated oxygen vacancies enhance the distortions of the host lattice [39].

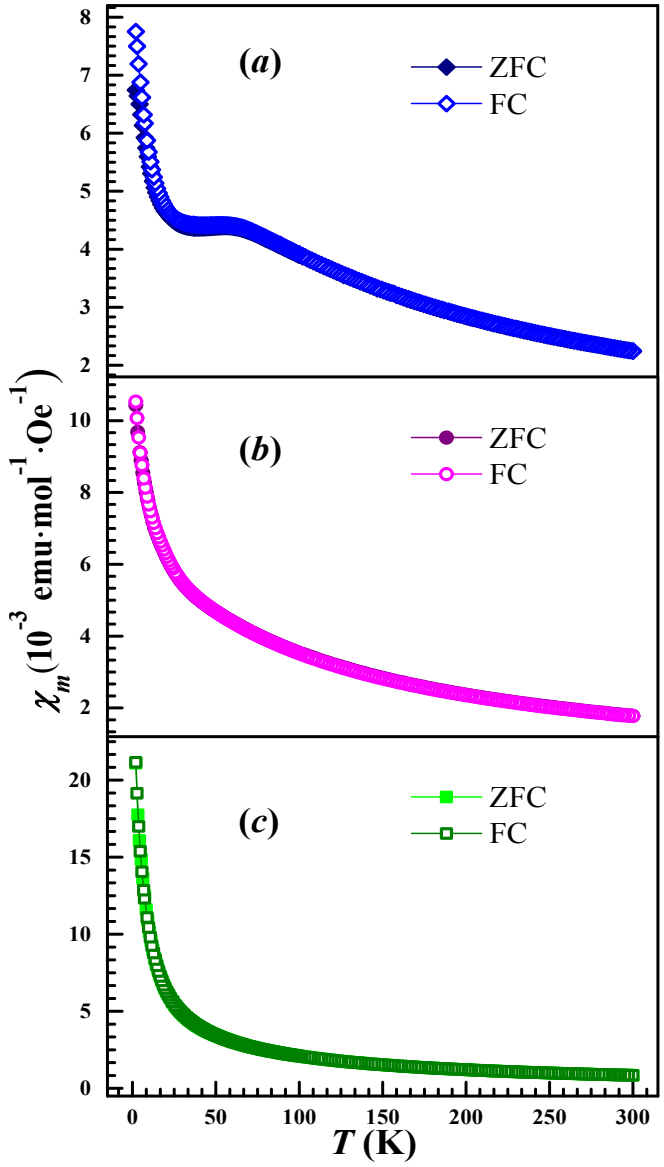

Fig. 6. Temperature dependence of the molar susceptibility of the $Sr_2Ni_{0.75}Mg_{0.25}MoO_6$ (*a*), $Sr_2Ni_{0.5}Mg_{0.5}MoO_6$ (*b*) and $Sr_2Ni_{0.25}Mg_{0.75}MoO_6$ (*c*) perovskites, measured in 1 kOe magnetic field.

Table 3
The results of analysis using the Curie-Weiss law: Curie-Weiss constant – C_p; Weiss paramagnetic temperature – θ_p; experimental and theoretical effective magnetic moment – μ_{eff}^{exp} of the $Sr_2Ni_{1-x}Mg_xMoO_6$ (x = 0, 0.25, 0.5, and 0.75).

Compound	T_N (K)	C_p (emu K mol^{-1} Oe^{-1})	θ_p (K)	μ_{eff}^{exp} (μ_B)
Sr_2NiMoO_6	82(1)	1.288(5)	−229.8 ± 2.1	3.22(1)
$Sr_2Ni_{0.75}Mg_{0.25}MoO_6$	55(1)	1.055(4)	−171.1 ± 1.5	2.92(1)
$Sr_2Ni_{0.5}Mg_{0.5}MoO_6$	–	0.717(3)	−102.8 ± 0.9	2.40(1)
$Sr_2Ni_{0.25}Mg_{0.75}MoO_6$	–	0.280(1)	−32.9 ± 0.3	1.503(6)

Fig. 5 shows the Raman spectra of the $Sr_2Ni_{1-x}Mg_xMoO_6$ (x = 0, 0.25, 0.50, and 0.75) samples in the range (1100–1800) cm^{-1}. Particularly, Raman spectra show a very characteristic feature called the D-band (the D denoting disorder-induced), which is a symmetry breaking Raman peak that has no intensity in the absence of defects. It is worth noting that not only the D-band feature can be used to understand defects, but also the symmetry allowed G-band in the Raman spectra provides valuable information about defects especially when the impurity dopes the material by changing the bonding strength of the atomic species to the host atoms [40]. From Fig. 5, a very weak band at 1228 cm^{-1} and a strong band at 1553 cm^{-1}, are shown, corresponding to the well-documented D and G bands for the $Sr_2Ni_{1-x}Mg_xMoO_6$ (x = 0, 0.25, 0.50, and 0.75) samples. The D and G bands are ascribed to structure defects and the first-order scatterings. The I_D/I_G ratio is commonly used as a measure of the quality of the sample produced: a smaller I_D/I_G ratio corresponds to a higher quality structure or fewer defects [41]. The I_D/I_G ratios for samples produced by $Sr_2Ni_{0.75}Mg_{0.25}MoO_6$, Sr_2NiMoO_6, $Sr_2Ni_{0.50}Mg_{0.50}MoO_6$, and $Sr_2Ni_{0.25}Mg_{0.75}MoO_6$ were 0.2375, 0.3000, 0.3333, and 0.4736 respectively. A high I_D/I_G ratio of 0.4736 was obtained for $Sr_2Ni_{0.25}Mg_{0.75}MoO_6$, indicating that a low-quality structure was formed. The I_D/I_G ratio indicates that the order of samples was decreasing in the sequence $Sr_2Ni_{0.25}Mg_{0.75}MoO_6$ > $Sr_2Ni_{0.50}Mg_{0.50}MoO_6$ > Sr_2NiMoO_6 > $Sr_2Ni_{0.75}Mg_{0.25}MoO_6$. These results were in good agreement with the XRD analysis.

3.3. Magnetic properties

Fig. 6 shows the temperature dependence of the molar susceptibility ($\chi_m(T)$) of $Sr_2Ni_{1-x}Mg_xMoO_6$ (x = 0.25, 0.5, and 0.75) polycrystals measured in the ZFC−FC modes upon H = 1 kOe. The Sr_2NiMoO_6 sample undergoes a second-order transition from the antiferromagnetic phase to paramagnetic state at T_N = 82(1) K. The data are in good agreement with the literature [6].

The temperature dependence of the molar susceptibility is shown in Fig. 6*a* for the $Sr_2Ni_{0.75}Mg_{0.25}MoO_6$ sample, which indicates the appearance of antiferromagnetic ordering below the Néel temperature $T_N \approx 56(1)$ K. As can be seen from Fig. 6*a*, the molar susceptibility begins to increase below 30 K, which is quite common among similar materials [7]. This phenomenon corresponds to the paramagnetic tail, which arises due to the imperfection of the long-range antiferromagnetic ordering in the material, while there remain several of isolated regions of non ordered atoms, which behave like paramagnetics [7]. The antiferromagnetic-paramagnetic phase transition temperatures for the $Sr_2Ni_{1-x}Mg_xMoO_6$ (x = 0, 0.25, 0.5, and 0.75) are given in Table 3. In comparison with pure Sr_2NiMoO_6 – the 25 at. % doping for Mg decreases the Néel temperature (see Fig. 6*a* and Table 3).

In the samples doped by 50 and 75 at. % of magnesium, the shape of the temperature dependence of molar susceptibility corresponds to the typical susceptibility curve of a paramagnet (Fig. 6*b*, *c*) [42].

In addition, the temperature dependence of the magnetic susceptibility in the paramagnetic region was analyzed using the Curie-Weiss law [43]. Fig. 7 shows the temperature dependence of the inverse susceptibility $1/\chi_m$ for the $Sr_2Ni_{1-x}Mg_xMoO_6$ (x = 0.25, 0.5, and 0.75) samples. The results of the analysis are presented in Table 3. For all samples, the Weiss paramagnetic temperatures are negative, which indicates a mainly antiferromagnetic ordering.

According to Table 3, the paramagnetic Weiss temperature increases with a rise of the magnesium concentration, while the magnetic effective moment decreases, that indicates the samples become paramagnetic. This is due to the fact that high concentrations of magnesium ions in $Sr_2Ni_{1-x}Mg_xMoO_6$ destroy the magnetic order in the compounds. This is also confirmed by a change in the shape of temperature dependence of the molar susceptibility (see Fig. 7*b*, *c*).

The magnetization curves $M(H)$ measured at 2 and 300 K and the dependences on the Mg concentration are shown in Figs. 8 and 9, respectively. The magnetization curves as a function of the magnetic field for Sr_2NiMoO_6 and $Sr_2Ni_{0.75}Mg_{0.25}MoO_6$ demonstrate nearly linear behavior at 2 K and 300 K, indicating the presence of an antiferromagnetic ordering [7]. With an increase of the concentration of Mg ions, the shape of the curve changes, corresponding to the suppression of the magnetic order in the samples and their transition to a paramagnetic state, as shown in the molar susceptibility of Sr_2Ni_{1-}

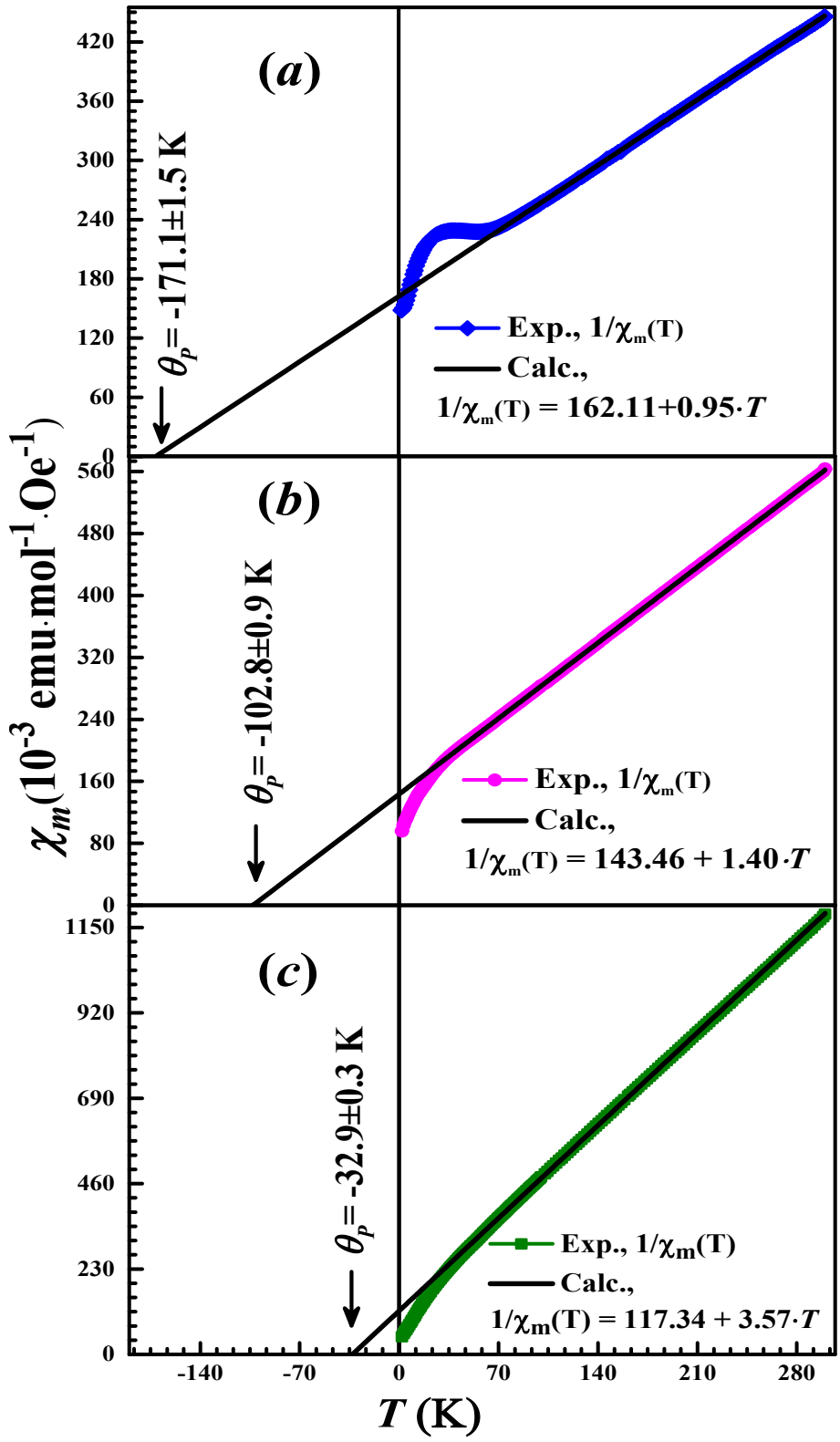

Fig. 7. The temperature dependence of inverse susceptibility of the $Sr_2Ni_{0.75}Mg_{0.25}MoO_6$ (*a*), $Sr_2Ni_{0.5}Mg_{0.5}MoO_6$ (*b*) and $Sr_2Ni_{0.25}Mg_{0.75}MoO_6$ (*c*) perovskites.

$_xMg_xMoO_6$ double perovskites. At the same time, there is a slight slope on the magnetization curves, this is especially noticeable for the $Sr_2Ni_{0.25}Mg_{0.75}MoO_6$ (Fig. 8). We assume that this is due to the appearance of weak ferromagnetism due to the destruction of the antiferromagnetic ordering and the slope of the nickel ion spins.

4. Conclusion

The $Sr_2Ni_{1-x}Mg_xMoO_6$ (x = 0, 0.25, 0.5, and 0.75) compositions with the double perovskite type structure were prepared via the glycerol-salt precursors route with the addition of ammonium nitrate as a combustion activator.

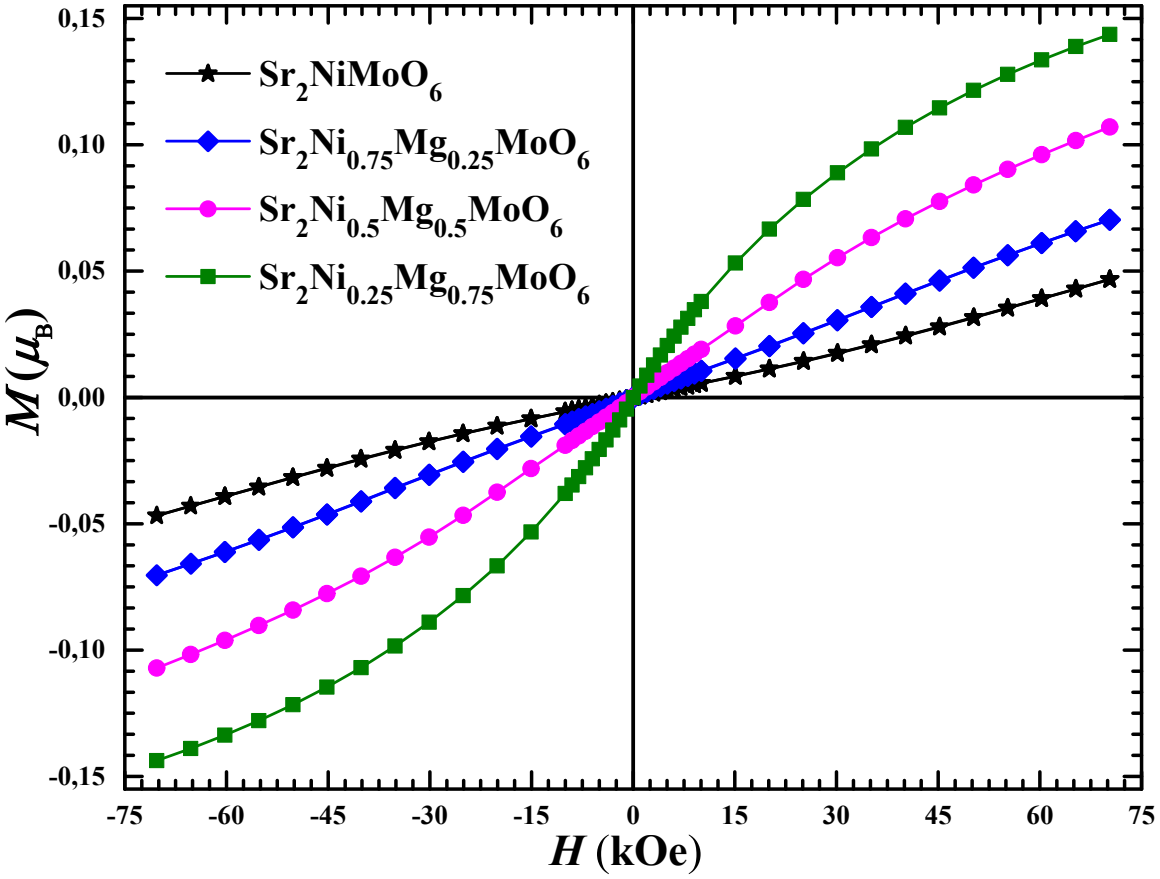

Fig. 8. Magnetization versus magnetic field of $Sr_2Ni_{1-x}Mg_xMoO_6$ (x = 0, 0.25, 0.5, and 0.75) at 2 K measured in magnetic field rang range ± 70 kOe.

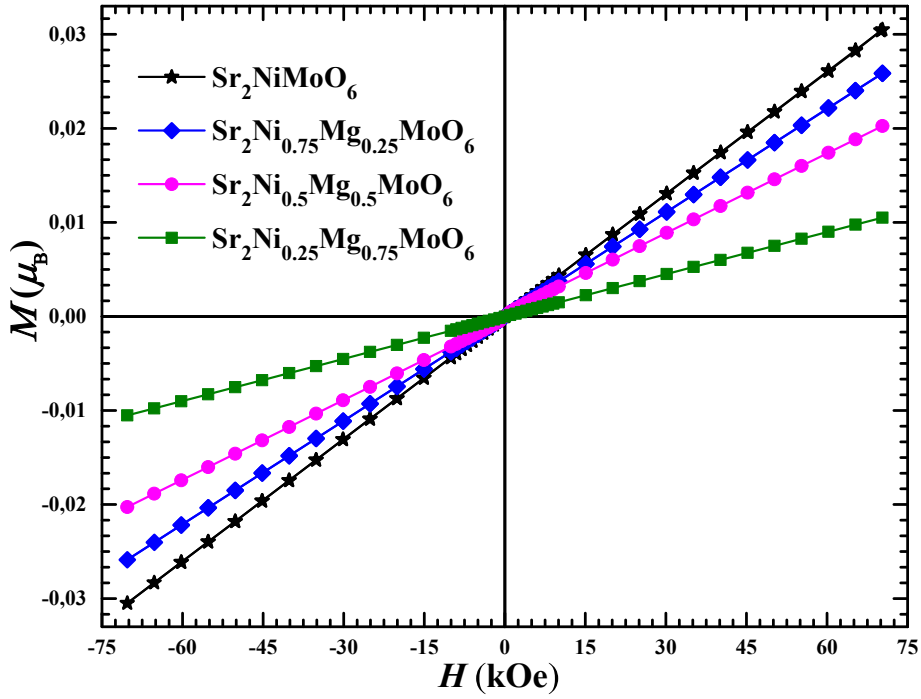

Fig. 9. Magnetization versus magnetic field of $Sr_2Ni_{1-x}Mg_xMoO_6$ (x = 0, 0.25, 0.5, and 0.75) at room temperature measured in magnetic field range ± 70 kOe.

The structure and magnetic properties of the $Sr_2Ni_{1-x}Mg_xMoO_6$ double perovskites have been studied with XRD, NPD, Raman scattering, and magnetic measurements. The polycrystals reveal a tetragonal symmetry. Raman analysis explains the structural changes with increasing the Mg concentration. Simultaneously with the increasing Mg, a decrease of antiferromagnetic spin correlations leading to the antiferromagnetic-paramagnetic transition and the 776 cm^{-1} peak indicates that there is evidence for structural transition from the

tetragonal (Sr_2NiMoO_6) to triclinic ($Sr_2Ni_{0.25}Mg_{0.75}MoO_6$) phase. This indicates also high purity of the $Sr_2Ni_{0.75}Mg_{0.25}MoO_6$ samples.

The susceptibility measurements of $Sr_2Ni_{0.75}Mg_{0.25}MoO_6$ suggest the establishment of antiferromagnetic interactions at $T_N \approx 56(1)$ K which is lower compared to that of pure Sr_2NiMoO_6 $T_N = 82(1)$ K.

The 50 and 75 at. % Mg doping suppresses the magnetic ordering and the samples become paramagnetic.

Acknowledgements

The research was carried out within the state assignment of Minobrnauki of Russia (theme "Flux" No. AAAA-A18-118020190112-8). The work was supported by MES of RF (contract No. 3.6121.2017/8.9), and by Act 211 Government of RF (contract No. 02.A03.21.0006).

References

[1] S. Vasala, M. Lehtimäki, Y.H. Huang, H. Yamauchi, J.B. Goodenough, M. Karppinen, Degree of order and redox balance in B-site ordered double-perovskite oxides, $Sr_2MMoO_{6-\delta}$ (M = Mg, Mn, Fe, Co, Ni, Zn), J. Solid State Chem. 183 (2010) 1007–1012.

[2] T. Wei, Y. Ji, X. Meng, Y. Zhang, $Sr_2NiMoO_{6-\delta}$ as anode material for $LaGaO_3$-based solid oxide fuel cell, J. Electrochem. Comm. 10 (2008) 1369–1372.

[3] N. Rezaei, T. Hashemifar, M. Alaei, F. Shahbazi, S.J. Hashemifar, H. Akbarzadeh, Ab initio investigation of magnetic ordering in the double perovskite Sr_2NiWO_6, Phys. Rev. B 99 (2019) 104411.

[4] C. Ritter, M.R. Ibarra, L. Morellon, J. Blasco, J. García, J.M. De Teresa, Structural and magnetic properties of double perovskites AA'$FeMoO_6$ (AA' = Ba_2, BaSr, Sr_2 and Ca_2), J. Phys. Condens. Matter 12 (2000) 8295–8308.

[5] S.A. Ivanov, S.-G. Eriksson, R. Tellgren, H. Rundlöf, M. Tseggai, The magnetoelectric perovskite Sr_2CoMoO_6: an insight from neutron powder diffraction, Mater. Res. Bull. 40 (2005) 840–849.

[6] A.K. Eriksson, S.-G. Eriksson, S.A. Ivanov, C.S. Knee, J. Eriksen, H. Rundlöf, M. Tseggai, High temperature phase transition of the magnetoelectric double perovskite Sr_2NiMoO_6 by neutron diffraction, Mater. Res. Bull. 41 (2006) 144–157.

[7] P. Kayser, M.J. Martínez-Lope, J.A. Alonso, M. Retuerto, M. Croft, A. Ignatov, M.T. Fernandez-Díaz, Crystal structure, phase transitions, and magnetic properties of iridium perovskites Sr_2MIrO_6 (M = Ni, Zn), Inorg. Chem. 52 (2013) 11013–11022.

[8] G. Blasse, Ferromagnetic interactions in non-metallic perovskites, J. Phys. Chem. Solids 26 (1965) 1969–1971.

[9] T. Kimura, H. Sawada, K. Terakura, Room-temperature magnetoresistance in an oxide material with an ordered double-perovskite structure, Nature 395 (1998) 677–680.

[10] B. Philipp, P. Majewski, L. Alff, A. Erb, R. Gross, T. Graf, M.S. Brandt, J. Simon, T. Walther, W. Mader, D. Topwal, D.D. Sarma, Structural and doping effects in the half-metallic double perovskite A_2CrWO_6 (A = Sr, Ba and Ca), Phys. Rev. B 68 (2003) 144431-13.

[11] S. Kumar, G. Giovannetti, J. van den Brink, S. Picozzi, Theoretical prediction of multiferroicity in double perovskite Y_2NiMnO_6, Phys. Rev. B 82 (2010) 134429–134436.

[12] J.B. Goodenough, Y.-H. Huang, Alternative anode materials for solid oxide fuel cells, J. Power Sources 173 (2007) 1–10.

[13] E.A. Filonova, A.S. Dmitriev, P.S. Pikalov, D.A. Medvedev, E.Y. Pikalov, The structural and electrical properties of $Sr_2Ni_{0.75}Mg_{0.25}MoO_6$ and its compatibility with solid state electrolytes, Solid State Ion. 262 (2014) 365–369.

[14] P. Kumar, Effect of lanthanum (La^{3+}) doping on the structural and electrical properties of double perovskite Sr_2NiMoO_6, RSC Adv. 6 (2016) 22094–22102.

[15] Z. Xie, H. Zhao, Z. Du, T. Chen, N. Chen, Electrical, chemical, and electrochemical properties of double perovskite oxides $Sr_2Mg_{1-x}Ni_xMoO_{6-\delta}$ as anode materials for solid oxide fuel cells, J. Phys. Chem. C 118 (2014) 18853–18860.

[16] P. Kumar, N.K. Singh, A.S.K. Sinha, P. Singh, Structural and electrical characterizations of cerium (Ce^{3+})-doped double perovskite system $Sr_2NiMoO_{6-\delta}$, Appl. Phys. A 122 (2016) 828–838.

[17] D.I. Khomskii, Multiferroics: different ways to combine magnetism and ferroelectricity, J. Magn. Magn. Mater. 306 (2006) 1–8.

[18] S.-W. Cheong, M. Mostovoy, Multiferroics: a magnetic twist for ferroelectricity, Nat. Mater. 6 (2007) 13–20.

[19] E.A. Filonova, O.V. Russkikh, L.S. Skutina, N.A. Kochetova, D.V. Korona, A.A. Ostroushko, Influence of synthesis conditions on phase formation and functional properties of prospective anode material $Sr_2Ni_{0.75}Mg_{0.25}MoO_{6-\delta}$, J. Alloy. Comp. 748 (2018) 671–678.

[20] P.K. Dager, C.M. Chanquía, L. Mogni, A. Caneiro, Synthesis of pure-phase Sr_2MgMoO_6 nanostructured powder by the combustion method, Mater. Lett. 141 (2015) 248–251.

[21] J. Rodriguez-Carvajal, Recent advances in magnetic structure determination by neutron powder diffraction, Physica B 192 (1993) 55–69.

[22] K. Momma, F. Izumi, VESTA: a three-dimensional visualization system for electronic and structural analysis, J. Appl. Crystallogr. 41 (2008) 653–658.

[23] E.A. Filonova, A.S. Dmitriev, Physicochemical properties of potential cathode$La_{1-x}Ba_xMn_{1-y}Cr_yO_3$ and anode Sr_2NiMoO_6 materials for solid-oxide fuel cells, Eurasian Chem. Technol. J. 14 (2012) 139–145.

[24] L.S. Skutina, A.I. Vylkov, K.V. Grzhegorzhevskii, A.Y. Chuikin, A.A. Ostroushko, E.A. Filonova, Crystal structure and phase transitions of $Sr_2Ni_{1-y}Mg_yMoO_6$ solid solutions, Inorg. Mater. 53 (2017) 1293–1299.

[25] V.V. Sereda, D.S. Tsvetkov, A.L. Sednev, A.I. Druzhinina, D.A. Malyshkin, A.Y. Zuev, Thermodynamics of Sr_2NiMoO_6 and Sr_2CoMoO_6 and their stability under reducing conditions, Phys. Chem. Chem. Phys. 20 (2018) 20108–20116.

[26] R.D. Shannon, C.T. Prewitt, Effective ionic radii in oxides and fluorides, Acta Crystallogr. 25 (1969) 925–946.

[27] D. Marrero-Lopez, J. Pena-Martinez, J.C. Ruiz-Morales, M.C. Martin-Sedeno, P. Nunez, High temperature phase transition in SOFC anodes based on $Sr_2MgMoO_{6-\delta}$, J. Solid State Chem. 182 (2009) 1027–1034.

[28] F.K. Patterson, C.W. Moeller, R. Ward, Magnetic oxides of molybdenum(V) and tungsten(V) with the ordered perovskite structure, Inorg. Chem. 2 (1963) 196–198.

[29] N. Setter, I. Laulicht, The observation of B-site ordering by Raman scattering in A(B′B″)O_3 perovskites, Appl. Spectrosc. 41 (1987) 526–528.

[30] U. Bismayer, V. Devarajan, P. Grooves, Hard-mode Raman spectroscopy and structural phase transition in the relaxor ferroelectric lead scandium tantalate, Pb$(Sc_{0.5}Ta_{0.5})O_3$, J. Phys. Condens. Matter 1 (1989) 6977–6986.

[31] C. Boulesteix, C. Caranoni, C.Z. Kang, L.M. Sapozhnikova, I.G. Siny, T.A. Smirnova, On the structural study of Pb_2ScTaO_6-type crystals by analytical electron microscopy and Raman scattering, Ferroelectrics 107 (1990) 241–246.

[32] I.G. Siny, R.S. Katiyar, A.S. Bhalla, Cation arrangement in the complex perovskites and vibrational spectra, J. Raman Spectrosc. 29 (1998) 385–390.

[33] Y.E. Chenzhou, Y. Jie, Y. Lixiu, C. Nianyi, Regularities of formation and lattice distortion of perovskite-type compounds, Chin. Sci. Bull. 47 (2002) 458–460.

[34] E.A. Filonova, A.S. Dmitriev, Crystal structure and thermal properties of Sr_2ZnMoO_6, Inorg. Mater. 49 (2013) 642–646.

[35] D. Chen, M. Liu, L. Yin, T. Li, Z. Yang, X. Li, B. Fan, H. Wang, R. Zhang, Z. Li, H. Xu, H. Lu, D. Yang, J. Sune, L. Gao, Single-crystalline MoO_3 nanoplates: topochemical synthesis and enhanced ethanol-sensing performance, J. Mater. Chem. 21 (2011) 9332–9342.

[36] N. Mironova-Ulmane, A. Kuzmin, I. Steins, J. Grabis, I. Sildos, M. Pärs, Raman scattering in nanosized nickel oxide NiO, J. Phys. Conf. Ser. 93 (2007) 012039–012045.

[37] M. Press, M. Mayer, P. Knoll, S. Lo, U. Hohenester, E. Holzinger-Schweiger, Magnetic Raman scattering in undoped and doped antiferromagnets, J. Raman Spectrosc. 27 (1996) 343–349.

[38] R.D. Shannon, Revised effective ionic radii and systematic studies of interatomic distances in halides and chaleogenides, Acta Crystallogr. A32 (1976) 751–767.

[39] P. Colomban, A. Slodczyk, Raman intensity: an important tool to study the structure and phase transitions of amorphous/crystalline materials, Opt. Mater. 31 (2009) 1759–1763.

[40] P.T. Araujo, M. Terrones, M.S. Dresselhaus, Defects and impurities in graphene-like materials, Mater. Today 15 (2012) 98–109.

[41] W.-W. Liu, A. Aziz, S.-P. Chai, A.R. Mohamed, U. Hashim, Synthesis of single-walled carbon nanotubes: effects of active metals, catalyst supports, and metal loading percentage, J. Nanomater. 2013 (2013) 1–8.

[42] D.A. Osinkin, E.V. Zabolotskaya, D.G. Kellerman, A.Y. Suntsov, The physical properties and electrochemical performance of Ca-doped $Sr_2MgMoO_{6-\delta}$ as perspective anode for solid oxide fuel cells, J. Solid State Electrochem. 22 (2018) 1209–1215.

[43] S.V. Vonsovsky, Magnetism, Nauka, Moscow, 1984.